Materials Today Chemistry 35 (2024) 101874

Contents lists available at ScienceDirect

Materials Today Chemistry

journal homepage: www.journals.elsevier.com/materials-today-chemistry/

In situ doped $Cs_2AgIn_{0.9}Bi_{0.1}Cl_6$:8%Yb,2%Er/PVDF composite films for the printing of multimodal fluorescent anti-counterfeiting marks

Jindou Shi [a], Zeyu Wang [b,**], Nikolai V. Gaponenko [c], Zheyuan Da [a], Chen Zhang [a], Junnan Wang [a], Yongqiang Ji [a], Qing Yao [a], Yusong Ding [a], Minqiang Wang [a], Youlong Xu [a,*]

[a] Electronic Materials Research Laboratory, Key Laboratory of the Ministry of Education International Center for Dielectric Research&Shannxi Engineering Research Center of Advanced Energy Materials and Devices, Xi'an Jiaotong University, 710049 Xi'an, China
[b] Frontier Institute of Science and Technology (FIST), Xi'an Jiaotong University, Xi'an 710049, Shaanxi, China
[c] Belarusian State University of Informatics and Radioelectronics, P. Browki 6, 220013 Minsk, Belarus

ARTICLE INFO

Keywords:
Anti-counterfeiting
Lead-free double perovskite
Polyvinylidene difluoride
Composite films
Multimodal fluorescent

ABSTRACT

The fluorescent anti-counterfeiting technology has become one of the most desirable candidates in practical anti-counterfeiting applications owing to its adjustable emission, high recognition and design flexibility. However, the security level of single emitting fluorescent materials was lower, and no longer able to cope with current forgery techniques, so the development of higher level multimodal fluorescent anti-counterfeiting technologies was urgent. In this report, lead-free double perovskite (DP) material $CsAgBiCl_6$ was chosen as the host and a technique for in situ growth in polymer polyvinylidene difluoride (PVDF) was proposed to obtain large-scale high-quality $Cs_2AgBiCl_6$/PVDF composite films (CFs). Subsequently, the $Cs_2AgIn_{0.9}Bi_{0.1}Cl_6$:8%Yb,2%Er/PVDF CFs with both down-conversion and up-conversion optical properties was achieved by hybrid (In^{3+}/Yb^{3+}/Er^{3+}) doping, which was able to displayed inconsistent fluorescence emission (orange and green) under different excitation sources, and their fluorescence intensities exhibited tunability with the change of the environmental temperature, greatly enhancing its competitiveness in the field of fluorescent anti-counterfeiting. Finally, different anti-counterfeiting marks have been designed by the screen-printing process, and the complex encryption once again ensured the security of the information, while bringing a new gospel to the subsequent development of lead-free DP materials.

1. Introduction

Ensuring the quality of products through anti-counterfeiting identification has become a common technical tool [1,2]. Over the past few decades, researchers have been working to develop a variety of advanced anti-counterfeiting technologies to solve the problem of forgery, including proton, magnetic, luminescent and hologram techniques [3–6]. Among these, fluorescent anti-counterfeiting technology has been widely praised, benefiting from the adjustable fluorescence emission and the strong photoluminescent intensity that can be easily identified, thereby providing a high level of security for the products [7,8]. However, accompanied by the progress of science and technology, counterfeiting technology has also gained further development, and the traditional single-color fluorescent anti-counterfeiting printing can no longer be satisfied with the security of product quality. Therefore, in order to upgrade the level of security and eliminate the risk of counterfeiting, more complex multimodal fluorescent anti-counterfeiting technology must be developed [9–11]. Currently, phosphors based on rare earth (RE) ions doping have been commonly applied in the field of fluorescent anti-counterfeiting, where multimodal fluorescence emission was achieved by compositing up conversion (UC) luminescent materials with down conversion (DC) fluorescent materials [12–14]. Unfortunately, this anti-counterfeiting process can be tedious, and the stability of different materials can be variable, resulting in uncoordinated fluorescence emission under long-term application, thereby failing to guarantee anti-counterfeiting accuracy [15–17]. Therefore, integrated UC and DC optical properties within the single host to obtain multimodal fluorescence emission will provide a new option for information security guaranteed.

It is well known that the more popular UC fluorescence emission was

* Corresponding author.
** Corresponding author.
E-mail addresses: zeyu.wang@xjtu.edu.cn (Z. Wang), ylxu@xjtu.edu.cn (Y. Xu).

https://doi.org/10.1016/j.mtchem.2023.101874
Received 2 August 2023; Received in revised form 24 November 2023; Accepted 19 December 2023
Available online 25 December 2023

achieved mainly through the doping of RE ions in oxides and fluorides, but the DC fluorescence emission cannot be guaranteed at this point [18, 19]. Similarly, quantum dots with excellent DC optical properties suffered from the lack of UC fluorescence due to the fact that RE ions were not readily doped [20–22]. Fortunately, the researchers found that the lead-free double perovskite (DP) $Cs_2B(I)B(III)Cl_6$ material possessed excellent optical properties and stability, and that the ion in the B (III)-site had the same valence and similar radius to the RE ions, which facilitated the doping of rare earth ions into the host [23–26]. In previous studies, efficient multimodal fluorescence emission was accomplished by co-doping $Yb^{3+}/Er^{3+}/Bi^{3+}$ into $Cs_2Ag_{0.6}Na_{0.4}InCl_6$ lead-free DP material, but its preparation required slowly crystallizing at high temperature (185 °C) for 45 h with hydrochloric acid concentration as solvent, and pre-grinding and refining before it could be utilized for subsequent anti-counterfeit printing [27]. Meanwhile, the lead-free DP nanomaterials (NCs) prepared by the traditional colloidal solution method need to be mixed with the polymer solution during the anti-counterfeiting printing process, and the stability of bare DP NCs was easily affected by the external environment, which requires further treatment of the lead-free DP nanomaterials [28–30]. It can be seen that these preparation processes are complex and low-yield, which are not suitable for large-scale anti-counterfeiting printing applications, so there was an urgent need for a convenient, low-cost and high-yield preparation strategy to obtain lead-free DP materials with multimodal fluorescent anti-counterfeiting.

Herein, lead-free DP $Cs_2AgBiCl_6$ was selected as the host, which was dissolved in a precursor solution of polymer polyvinylidene difluoride (PVDF) to obtain the $Cs_2AgBiCl_6$/PVDF composite films (CFs) by an in-situ growth strategy, and the whole preparation only required annealing at 180 °C for 1h to achieve large size CFs, which will facilitate subsequent commercial production. Unfortunately, the inherent indirect band gap of $Cs_2AgBiCl_6$ severely limited the DC fluorescence emission of the CFs. Subsequently, the band gap was adjusted and the optical properties was optimized by in situ doping of In^{3+}, yielding $Cs_2AgIn_{0.9}Bi_{0.1}Cl_6$/PVDF CFs that emitted bright orange under 365 nm ultraviolet (UV) light excitation. Further, in order to develop the UC fluorescence emission of CFs, $Cs_2AgIn_{0.9}Bi_{0.1}Cl_6$:8%Yb,2%Er/PVDF CFs was obtained by again in situ doping with a mixture of Yb and Er, which was able to emit a bright green under 980 nm infrared (IR) light excitation, while retaining the DC fluorescence properties. Moreover, the temperature-dependent photoluminescence (PL) spectra of $Cs_2AgIn_{0.9}Bi_{0.1}Cl_6$:8% Yb,2%Er/PVDF CFs were recorded, and its UC and DC PL intensities exhibited different tendency as the environmental temperature increased, which caused the composite film to be shown additional encrypted behaviors, contributing to the improvement of anti-counterfeiting capability. Finally, the screen-printing technique was adopted to produce an anti-counterfeiting mark with excellent multimodal fluorescence properties, which once again confirmed the promising application of $Cs_2AgIn_{0.9}Bi_{0.1}Cl_6$:8%Yb,2%Er/PVDF CFs in the field of fluorescent counterfeiting, bringing a new dawn to the next generation of information security.

2. 2. Results and discussion

$Cs_2AgIn_xBi_{1-x}Cl_6$/PVDF CFs with different In^{3+} content was obtained by employing a simple in-situ preparation strategy, followed by the structure and micro-morphology of these CFs were further investigated with x-ray diffraction (XRD), scanning electron microscope (SEM), and energy-dispersive spectroscopy (EDS) analysis. XRD patterns of $Cs_2AgIn_xBi_{1-x}Cl_6$/PVDF CFs with different In^{3+} content showed that all samples crystallized in the DP structure, where the diffraction peaks were located between the bulk $Cs_2AgInCl_6$ (ICSD: 257115) and the bulk $Cs_2AgBiCl_6$ (ICSD: 291598) (Fig. 1a). At the same time, two additional diffraction peaks were observed at 18° and 19°, which belong to PVDF, preliminarily confirming the composite of $Cs_2AgIn_xBi_{1-x}Cl_6$ and PVDF to be completed. Subsequently, XRD patterns in the range 23°–25° were magnified for observation to understand the influence of In^{3+} doping on the $Cs_2AgBiCl_6$ structure. The diffraction peaks of $Cs_2AgIn_xBi_{1-x}Cl_6$/PVDF CFs shifted toward higher 2θ angles as the In^{3+} content increased, which was explained by the lattice contraction induced by the substitution of Bi^{3+} (ionic radius of 117 p.m.) with the smaller In^{3+} (94 p.m.) [31]. The corresponding SEM images revealed basically the same morphology of $Cs_2AgIn_xBi_{1-x}Cl_6$/PVDF (x = 0 %, 90 %, 100 %) CFs (Fig. 1b–d), where $Cs_2AgIn_xBi_{1-x}Cl_6$ particles with an average particle size of 200 nm were composited with PVDF, indicating that the in-situ growth of $Cs_2AgIn_xBi_{1-x}Cl_6$ in PVDF had been achieved by this simple

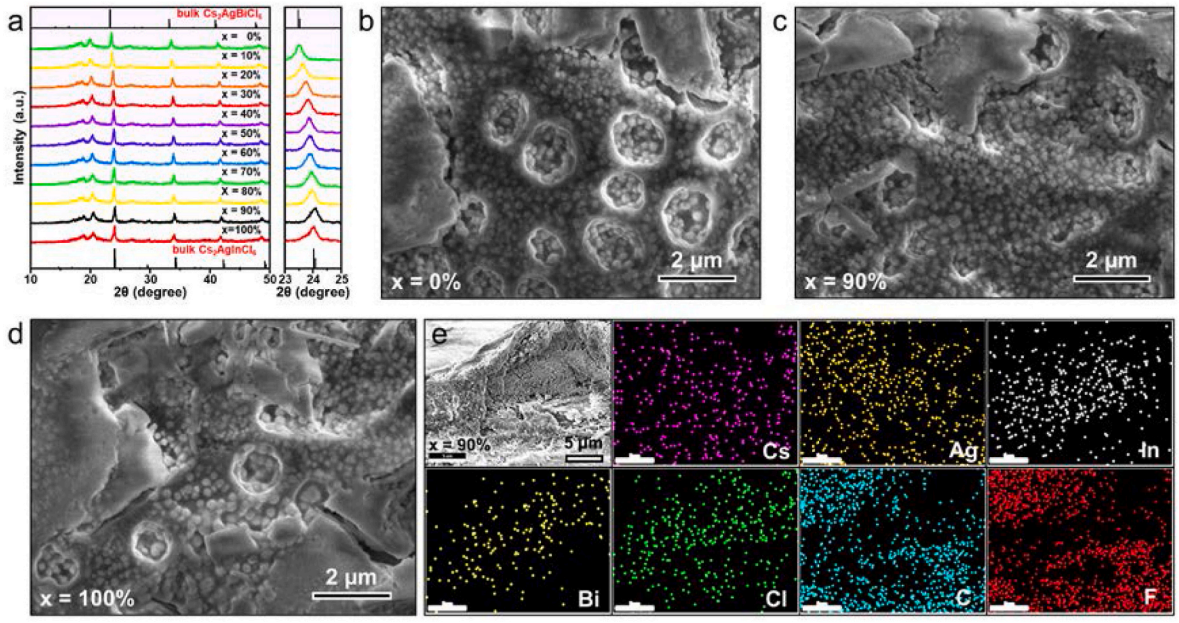

Fig. 1. (a) XRD patterns of $Cs_2AgIn_xBi_{1-x}Cl_6$/PVDF CFs with different In^{3+} content (the bottom corresponds to a pure bulk $Cs_2AgInCl_6$ (ICSD: 257115) and the top to a pure bulk $Cs_2AgBiCl_6$ (ICSD: 291598). SEM images of (b) $Cs_2AgBiCl_6$/PVDF CFs, (c) $Cs_2AgIn_{0.9}Bi_{0.1}Cl_6$/PVDF CFs and (d) $Cs_2AgInCl_6$/PVDF CFs. (e) Elemental mapping of $Cs_2AgIn_{0.9}Bi_{0.1}Cl_6$/PVDF CFs.

preparation strategy. Finally, the elemental mapping of $Cs_2AgIn_{0.9}Bi_{0.1}Cl_6$/PVDF CFs indicated that the different elements were uniformly distributed in the CFs (Fig. 1e), which again reflected that hybrid DP particles were already formed in PVDF matrix. Combined with the above characterization results, the high quality of $Cs_2AgIn_xBi_{1-x}Cl_6$/PVDF CFs can be achieved directly by this simple in-situ preparation strategy, which will pave the way for the subsequent commercial development of DP materials.

Firstly, the DC optical properties of $Cs_2AgIn_xBi_{1-x}Cl_6$/PVDF CFs were explored in depth, thereby laying the foundation for their subsequent development in the field of optical anti-counterfeiting. The UV–Vis absorbance spectra indicated a strong exciton absorption peak at 370 nm for pure $Cs_2AgBiCl_6$/PVDF CFs (Fig. 2a), which originated from the s→p transition of Bi^{3+} [32], indicating that they can capture high energy UV light, thereby ensuring their down-conversion fluorescence emission behavior. Meanwhile, the $Cs_2AgBiCl_6$/PVDF CFs exhibited a long sub-bandgap absorption tail at 400–700 nm (Fig. 2a), which mainly derived from trap-state related and indirect bandgap transitions [33,34], and similar phenomena have been reported in previous nanocrystals (NCs) [35]. The indirect bandgap nature of $Cs_2AgBiCl_6$/PVDF CFs has caused its fluorescent emission intensity to be lower (Fig. 2b), severely limiting further optical exploitation, so that the pure phase $Cs_2AgBiCl_6$/PVDF CFs would not be suitable for optical anti-counterfeiting. Contrastingly, no significant absorption peaks were observed in the absorbance spectrum of the pure $Cs_2AgInCl_6$/PVDF CFs, but they exhibited a weaker optical absorption coefficient around the band gap (Fig. S1a), thus also exhibiting no noticeable PL emission (Fig. S1c), which was consistent with the optical properties of the $Cs_2AgInCl_6$ NCs [36]. As can be seen, both pure $Cs_2AgBiCl_6$/PVDF CFs and $Cs_2AgInCl_6$/PVDF CFs cannot be promoted in practical applications owing to their poor fluorescence emission, so the emphasis will be on the optical properties of doped $Cs_2AgIn_xBi_{1-x}Cl_6$/PVDF CFs (x from 10 % to 90 %). Undoubtedly, a significant exciton absorption peak at 370 nm was also observed in the absorbance spectra of $Cs_2AgIn_xBi_{1-x}Cl_6$/PVDF CFs (x from 10 % to 90 %), stemming from the existence of Bi^{3+} in the host (Fig. 2a). Moreover, the absorption tail was gradually suppressed as the In^{3+} content in CFs increased, and the band edges of the corresponding absorbance spectra became sharp when the In^{3+} content reached 90 %, thereby demonstrating that the doping of In^{3+} modified the energy band structure of $Cs_2AgBiCl_6$ [31]. At the same time, an orange emission peak at 570 nm was detected in the PL spectra of $Cs_2AgIn_xBi_{1-x}Cl_6$/PVDF CFs (x from 10 % to 90 %) (Fig. 2b), resulting from the self-trapping exciton (STE) state PL emission, where $Cs_2AgIn_{0.9}Bi_{0.1}Cl_6$/PVDF CFs possessed the highest PLQYs at 46.18 %. The PL excitation (PLE) spectrum corresponding to $Cs_2AgIn_{0.9}Bi_{0.1}Cl_6$/PVDF CFs was consistent with the absorbance spectrum, showing a strong absorption for the 370 nm light source (Fig. S2a). The PLE mapping revealed that the fluorescence emission peak of $Cs_2AgIn_{0.9}Bi_{0.1}Cl_6$/PVDF CFs does not changed with the excitation source, which would be typical of STE PL emission (Fig. S2b) [37]. Subsequently, the corresponding time-resolved PL

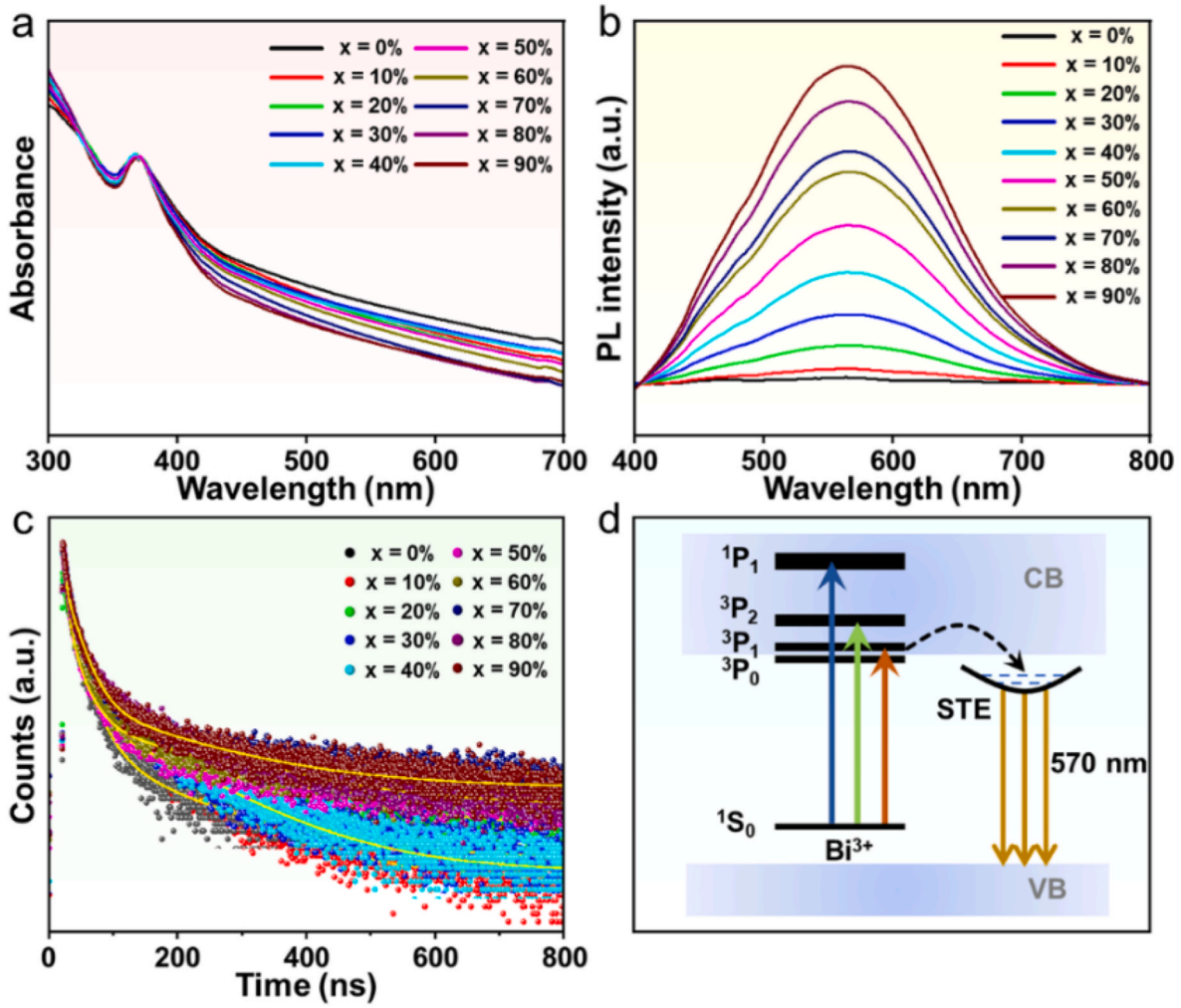

Fig. 2. (a) Absorbance and (b) PL spectra of $Cs_2AgIn_xBi_{1-x}Cl_6$/PVDF CFs as the In^{3+} content increased. (c) Time-resolved PL spectra and fitted curves for CFs with different In^{3+} content. (d) Energy-level diagram of In^{3+}-doped $Cs_2AgBiCl_6$/PVDF CFs and the DC PL mechanism (CB, conduction band; VB, valence band; STE, self-trapped exciton state).

spectra were recorded in order to better analyzed the influence for In^{3+} on the carrier dynamics of $Cs_2AgIn_xBi_{1-x}Cl_6$/PVDF CFs (Fig. 2c). The fitting results showed that the PL decay lifetime of $Cs_2AgIn_{0.9}Bi_{0.1}Cl_6$/PVDF CFs was 91.47 ns (Table S1), which was much higher than that of $Cs_2AgBiCl_6$/PVDF CFs (47.65 ns). It can be seen that the doping of In^{3+} prolonged the carrier lifetime by about two times, which was attributed to the In^{3+} addition promoting the formation of STEs, and a similar phenomenon was found in the report on lead-free DP nanocrystals [28,29]. Combined the above optical characterization analysis, the possible mechanism of DC PL in doped $Cs_2AgIn_xBi_{1-x}Cl_6$/PVDF CFs was proposed (Fig. 2d). The excitation energy was absorbed by Bi^{3+} ions in $Cs_2AgIn_xBi_{1-x}Cl_6$, which included three types of transitions, the dipole allowed transition of $^1S_0 \rightarrow {}^1P_1$, the spin orbital allowed transitions of $^1S_0 \rightarrow {}^3P_1$, and the forbidden transition of $^1S_0 \rightarrow {}^3P_2$ [25,38]. Benefiting from the doping of In^{3+} ions, the energy band structure of $Cs_2AgBiCl_6$ was modified, thereby inducing the forbidden transition of Bi^{3+} to be broken, allowing dramatically enhanced absorption of the transition, a large amount of effective energy being transferred to the STE state, followed by the emission of bright orange light at 570 nm.

To better understand the origin of the orange light emission in $Cs_2AgIn_xBi_{1-x}Cl_6$/PVDF CFs, the Perdew-Burke-Ernzerhof (PBE)-DFT calculations considering spin-orbit coupling (SOC) effects were carried out, resulting in the electronic structure of $Cs_2AgIn_xBi_{1-x}Cl_6$. Here, the crystal structures of $Cs_2AgIn_xBi_{1-x}Cl_6$ were investigated under four different doping conditions, pure phase $Cs_2AgBiCl_6$ (Fig. 3a), $Cs_2AgIn_{0.25}Bi_{0.75}Cl_6$ (small amount of In^{3+} doping) (Fig. 3b), $Cs_2AgIn_{0.75}Bi_{0.25}Cl_6$ (excess amount of In^{3+} doping) (Fig. 3c) and pure phase $Cs_2AgInCl_6$ (Fig. 3d), respectively. According to the corresponding band structure calculations, it can be seen that the pure phase $Cs_2AgBiCl_6$ showed an indirect band gap (Fig. 3e), while the pure phase $Cs_2AgInCl_6$ displayed a direct band gap (Fig. 3h). Of these, $Cs_2AgBiCl_6$ had an indirect band gap of 1.798 eV from the *X* point to the *L* point, and the maximum valence band (VBM) consisted mainly of Cl-p, Ag-d and Bi-s orbitals, while the minimum conduction band (CBM) was formed mainly by Bi-p, Cl-p and Ag-s orbitals (Fig. S3a) [39]. $Cs_2AgInCl_6$ had a direct band gap of 1.057 eV, and both VBM and CBM were located at the G point, where VBM consisted of In-d, Cl-p and Ag-d, while CBM consisted of Ag-s, Cl-p and In-s (Fig. S3d) [35]. The optical transition between the band edge states at the G point was parity forbidden, and this parity forbidden transition was so weaker, resulting in its fluorescence emission being almost invisible. Moreover, the experimental bandgap of Cs_2AgICl_6 (3.85 eV, Figs. S1a and b) was much larger than the calculated result (1.057 eV), which was attributed to the fact that direct band transitions are parity forbidden (Fig. S1d), and similar reports have been found in previous studies [36,40,41]. Subsequently, the band structures of doping $Cs_2AgIn_{0.25}Bi_{0.75}Cl_6$ and $Cs_2AgIn_{0.75}Bi_{0.25}Cl_6$ were analyzed. As the In^{3+} doping concentration increased, the In-s orbitals were involved on the composition of the CBM in $Cs_2AgIn_{0.25}Bi_{0.75}Cl_6$ (Fig. 3f), which lowered the barrier and resulted in a decrease in the band gap of $Cs_2AgIn_{0.25}Bi_{0.75}Cl_6$. According to previous reports, mixing between Ag and Bi frontier orbitals in VBM and CBM has been identified as the source of the indirect band gap in Ag–Bi DP crystals, thus $Cs_2AgIn_{0.25}Bi_{0.75}Cl_6$ maintained the characteristics of the indirect band gap (1.771 eV) [35,42]. However, with the closer enhancement of the In^{3+} content, the VBM of $Cs_2AgIn_{0.75}Bi_{0.25}Cl_6$ had Cl-p Ag-d and Bi-s orbitals like the $Cs_2AgBiCl_6$ (Fig. 3e, g), and the CBM contained In-s, Cl-p, and Ag-s orbitals like the $Cs_2AgInCl_6$ (Fig. 2g and h), with the Bi-p orbit not being involved in the composition thereby maintained a high barrier, resulting in an increased band gap (2.021 eV) for $Cs_2AgIn_{0.75}Bi_{0.25}Cl_6$. At the same time, the CBM of $Cs_2AgIn_{0.75}Bi_{0.25}Cl_6$ was flat from G to Z, and these calculations suggest that $Cs_2AgIn_xBi_{1-x}Cl_6$ (x = 0.75) can undergo a direct transition at G (Fig. 2g). By combining their absorbance spectra, the direct transition exhibited by $Cs_2AgIn_{0.75}Bi_{0.25}Cl_6$ at the G point should be forbidden, because only a single absorption peak was observed in the absorbance spectra, which derived from the high-energy Bi^{3+} s→p direct transition. However, the parity forbidden transition only affected the absorption, not the relaxation of photoexcited electrons and holes in the forbidden state, resulting in orange light emission, which consistent with the previously mentioned DC PL mechanism (Fig. 2d). By the above comparison, the DC optical properties of $Cs_2AgIn_{0.9}Bi_{0.1}Cl_6$ with the largest In^{3+} ion content were most prominent, and for the convenience of subsequent studies, $Cs_2AgIn_{0.9}Bi_{0.1}Cl_6$/PVDF CFs will be abbreviated as CAIBC/PVDF CFs.

Subsequently, CAIBC/PVDF CFs with outstanding optical properties was selected for the investigation, and the preparation process was

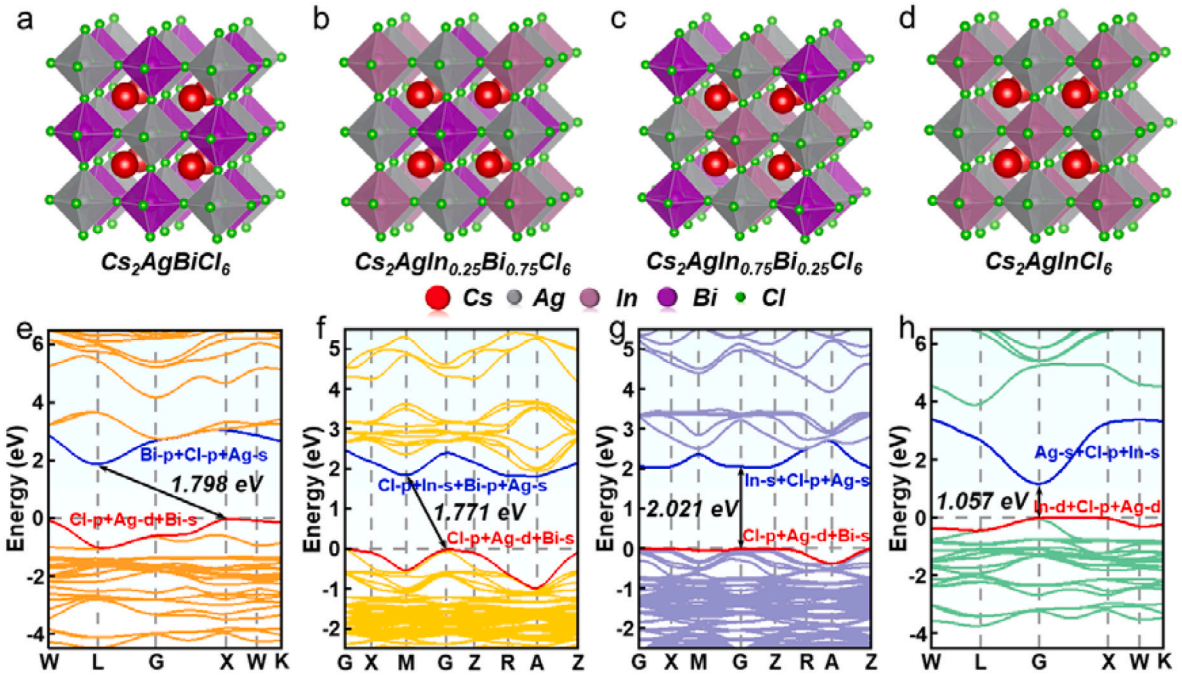

Fig. 3. (a–d) Crystal structure of $Cs_2AgIn_xBi_{1-x}Cl_6$ (x = 0 %, 25 %, 75 %, 100 %). (e–h) Band structure of $Cs_2AgIn_xBi_{1-x}Cl_6$ (x = 0 %, 25 %, 75 %, 100 %).

monitored closely, thereby providing a more comprehensive description on the doping process of $Cs_2AgIn_xBi_{1-x}Cl_6$ within PVDF. In this report, CFs with different components were obtained by in-situ preparation using a blade coater (Fig. 4a), where precursor I comprising all the elements of $Cs_2AgIn_xBi_{1-x}Cl_6$ was firstly acquired, followed by the addition of PVDF to get precursor II, and finally coated onto a heated substrate to complete the preparation of the doped CFs. Fig. 4b showed the control of temperature conditions during the heating to complete the doping of $Cs_2AgIn_xBi_{1-x}Cl_6$ in PVDF. The heated substrate was ramped up to 180 °C at 5 °C/min, followed by a constant temperature of 1 h at this temperature to facilitate the further maturation of $Cs_2AgIn_xBi_{1-x}Cl_6$, and finally natural cooling to room temperature yielding $Cs_2AgIn_xBi_{1-x}Cl_6$/PVDF CFs. Finally, the entire growth process of CAIBC/PVDF CFs with excellent PL properties was viewed in situ, providing insight into the crystallization dynamics of $Cs_2AgIn_{0.9}Bi_{0.1}Cl_6$ in PVDF by recording variations in its optical properties (Fig. 4c). The change in the thermal environment during the whole preparation process was captured using an infrared thermal imaging camera. When the temperature was elevated to 70 °C, the PVDF film was formed at this point, however there was no fluorescence emission under UV light, indicating that the $Cs_2AgIn_{0.9}Bi_{0.1}Cl_6$ within PVDF had not crystallized. Subsequently, the temperature was further increased to 130 °C, and the CFs emitted orange fluorescence under UV light, but the fluorescence intensity was weaker, indicating that $Cs_2AgIn_{0.9}Bi_{0.1}Cl_6$ had just started to be crystallized slowly. Immediately afterwards, the temperature reached the pre-set growth temperature (180 °C), the CFs remained emitting orange fluorescence under UV light, at which point the fluorescence intensity increased, suggesting that $Cs_2AgIn_{0.9}Bi_{0.1}Cl_6$ was further crystallized in PVDF. Finally, after the holding was finished, the fluorescence intensity of $Cs_2AgIn_{0.9}Bi_{0.1}Cl_6$/PVDF CFs was again intensified, at which point the entire CFs emitted bright orange light, demonstrating that $Cs_2AgIn_{0.9}Bi_{0.1}Cl_6$ in PVDF had been completely crystallized, achieving a large area of CAIBC/PVDF CFs with excellent optical properties. Additionally, in order to understand the influence of constant temperature time on film growth, the constant temperature time was extended to 70 min. Unfortunately, the surface PVDF layer showed non-uniform shrinkage owing to the rapid evaporation of the solvent. Meanwhile, large gaps appeared on the surface of the $Cs_2AgIn_{0.9}Bi_{0.1}Cl_6$/PVDF CFs, and the internal $Cs_2AgIn_{0.9}Bi_{0.1}Cl_6$ crystals were clustered together (Fig. S4a), which resulted directly to the optical emission non-uniformity and decay of PL emission intensity (Fig. S4b) from the film, a similar phenomenon was also reported in the previous preparation of $Cs_2Na_{0.8}Ag_{0.2}BiCl_6$/PMMA CFs [23]. By analyzing the in-situ growth process of $Cs_2AgIn_xBi_{1-x}Cl_6$ in PVDF, it will assist in the subsequent tuning of process parameters, thereby greatly boosting the development of $Cs_2AgIn_xBi_{1-x}Cl_6$/PVDF CFs in the commercial field.

In the next step, in order to achieving multimodal fluorescent anti-counterfeiting of CAIBC/PVDF CFs, the up-conversion (UC) PL properties were conferred the doping of rare earth ions (Yb^{3+}, Er^{3+}), which showed different fluorescence emission under short and long wavelength (UV and IR) excitation, thereby enhancing the security level. Interestingly, the rare earth ions were mostly trivalent, thus preferential equivalence substitution of the B(III)-site of lead-free DPs during the doping, where the B(III)-site would contain elements In, Bi, Yb and Er. Additionally, the ratio of In^{3+} and Bi^{3+} was maintained to guarantee that the DC optical properties of CAIBC/PVDF CFs would not be affected, and the content of Yb^{3+} and Er^{3+} was controlled to 10 % based on the results of previous studies [27,43,44]. The XRD pattern of CAIBC:(10%-y)Yb,yEr/PVDF CFs showed that the samples maintained the DP structure, and the doping did not induce a transformation in the crystalline phase (Fig. 5a). Subsequently, the XRD magnification in the range 23°–25° was viewed again, and the diffraction peaks of CAIBC:(10%-y)Yb,yEr/PVDF CFs can be seen shifted to lower 2θ angles as the Yb^{3+} content decreased, which can be attributed to the lattice expansion

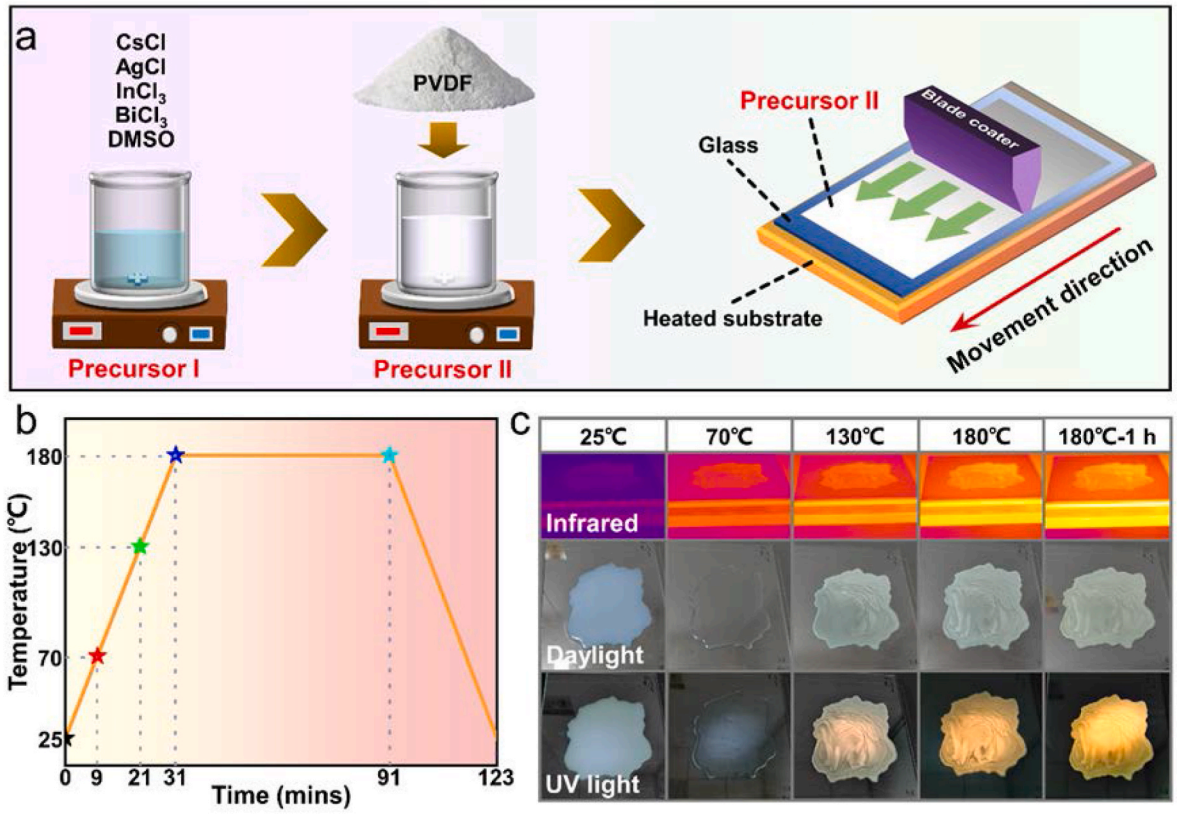

Fig. 4. (a) A schematic diagram for the preparation process of CAIBC/PVDF CFs. (b) Analytical diagram for in situ observation of the growth process in CAIBC/PVDF CFs. (c) Photographs of the corresponding CAIBC/PVDF CFs under daylight and 365 nm UV light during the growth process.

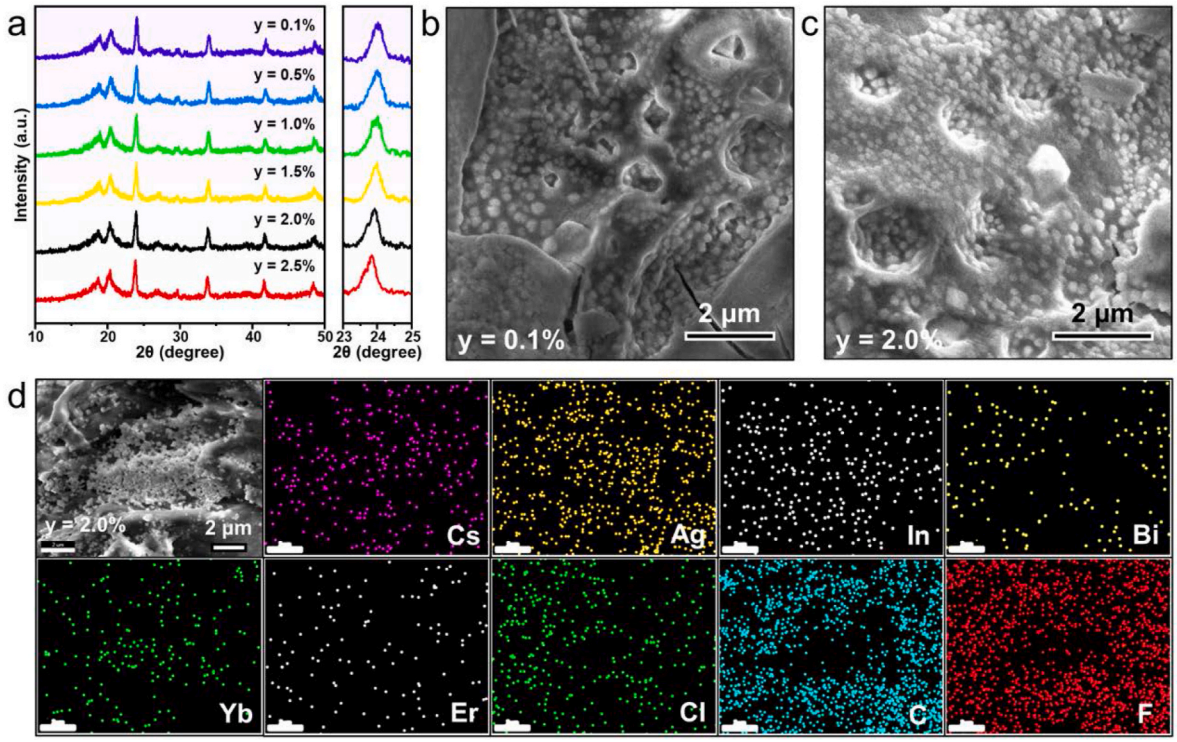

Fig. 5. (a) XRD patterns of CAIBC:(10%-y)Yb,yEr/PVDF CFs with different Er^{3+} content. SEM images of (b) CAIBC:9%Yb,1%Er/PVDF CFs and (c) CAIBC:8%Yb,2% Er/PVDF CFs. (d) Elemental mapping of CAIBC:8%Yb,2%Er/PVDF CFs.

resulting from the substitution of the smaller Yb^{3+} (100.8 p.m.) by Er^{3+} (103 p.m.) [45]. SEM images indicated that the morphology of the CFs were not significantly altered after the introduction of rare earth ions, and the average particle size of CAIBC:(10%-y)Yb,yEr with different ratios in PVDF remained at approximately 200 nm (Fig. 5b and c), which was essentially the same as $Cs_2AgIn_xBi_{1-x}Cl_6$ mentioned previously. Moreover, the elemental mapping of CAIBC:8%Yb,2%Er/PVDF CFs demonstrated a uniform distribution of all elements in the PVDF film (Fig. 5d), which again confirmed that the growth of hybrid CAIBC:8% Yb,2%Er in PVDF had been completed. Furthermore, the chemical state and quantitative analysis of all elements in CAIBC:8%Yb,2%Er/PVDF CFs were determined using X-ray photoelectron spectroscopy (XPS). As shown in Fig. S5, the XPS survey spectra identified characteristic peaks of all elements in CAIBC:8%Yb,2%Er/PVDF CFs. Of these, the Yb 4d and Er 4d characteristic peaks can be observed at 187.4 eV and 172.3 eV, respectively, which are consistent with the results of the XPS spectra for $NaGdF_4$:Yb,Er nanocrystals and $NaYF_4$: Yb, Er compounds [46,47], suggesting that the tri-valent Yb^{3+} and Er^{3+} have been doped completely into the $Cs_2AgIn_{0.9}Bi_{0.1}Cl_6$. Subsequently, the atomic percentages results showed that Yb and Er had the least percentage of atoms, while C and F atoms (the constituent elements of the PVDF film) had the most, which corresponded perfectly to the results obtained from the elemental mapping (Fig. 5d). Additionally, CAIBC:8%Yb,2%Er/PVDF CFs were obtained at different annealing temperatures to investigate the influence on the fluorescence properties of composite films from the preparation process. The crystallinity of CAIBC:8%Yb,2%Er in PVDF also increased with the annealing temperature, the grain size became larger, and the DC and UC fluorescence emission intensities were continuously enhanced (Figs. S6a–h). Unfortunately, the PVDF layer on the surface of composite films cannot withstand the high temperature when the annealing temperature reached 200 °C (Fig. S6f), hardening and shrinking, and flexible stretching was not possible, while the fluorescent properties of the composite films were reduced (Figs. S6g–h), so 180 °C became the preferred annealing temperature. Through the above morphological and structural analysis, the in-situ preparation strategy can be universally applied to the compositing of lead-free DP with polymeric materials, and its large-scale and convenient preparation process will bring new opportunities for the development of lead-free DP.

To confirm that CAIBC:(10%-y)Yb,yEr/PVDF CFs can be implemented for multimodal anti-counterfeiting, its DC and UC fluorescence properties were explored deeply. It can be seen that the doping of Yb^{3+} and Er^{3+} had virtually no influence on the DC fluorescence behaviors of CAIBC, where the main emission peak remained at 570 nm under 365 nm UV excitation (Fig. 6a), displaying bright orange emission, the corresponding color coordinates in the International Commission on illumination (CIE) diagram being (0.38, 0.43) (Fig. 6f). Interestingly, a weaker shoulder peak at 523 nm was observed in the DC PL spectrum of CAIBC:7.5%Yb,2.5%Er/PVDF CFs when the Er^{3+} content reached 2.5 %, which corresponded exactly to the $^2H_{11/2} \rightarrow {}^4I_{15/2}$ transition of Er^{3+} (Fig. 6a). At the same time, the DC PL mechanism of CAIBC:(10%-y)Yb, yEr/PVDF CFs will be changed, with the energy absorbed by Bi^{3+} being transferred to the STE state and then partially shifted to $^2H_{11/2}$ of Er^{3+}, thereby yielding additional emission at 523 nm (Fig. 6g). Subsequently, it was further investigated the UC optical properties of CAIBC:(10%-y) Yb,yEr/PVDF CFs with different components. Under the excitation of the 980 nm IR laser, the UC PL spectra of all samples showed three distinct emission peaks located at 523 nm, 550 nm and 660 nm, which were derived from the $^2H_{11/2} \rightarrow {}^4I_{15/2}$ transition, $^2S_{3/2} \rightarrow {}^4I_{15/2}$ transition and $^4F_{9/2} \rightarrow {}^4I_{15/2}$ transition of Er^{3+}, respectively (Fig. 6b). Moreover, the UC PL intensity of CAIBC:(10%-y)Yb,yEr/PVDF CFs gradually enhanced as the Er content increased, and the emission intensity was maximized when the Er content was 2.0 %, where CAIBC:8%Yb,2%Er/PVDF CFs displayed green light emission, corresponding to the color coordinates (0.26, 0.71) (Fig. 6f). However, the emission intensity of CAIBC:7.5% Yb,2.5%Er/PVDF CFs dropped again as the Er content continued to be elevated, which was attributed to a concentration quenching effect, a similar phenomenon being found in other UC fluorescent materials [48, 49]. Afterwards, the PL decay lifetimes of the samples at the main emission peak of 523 nm were recorded (Fig. 6c), and the decay lifetime

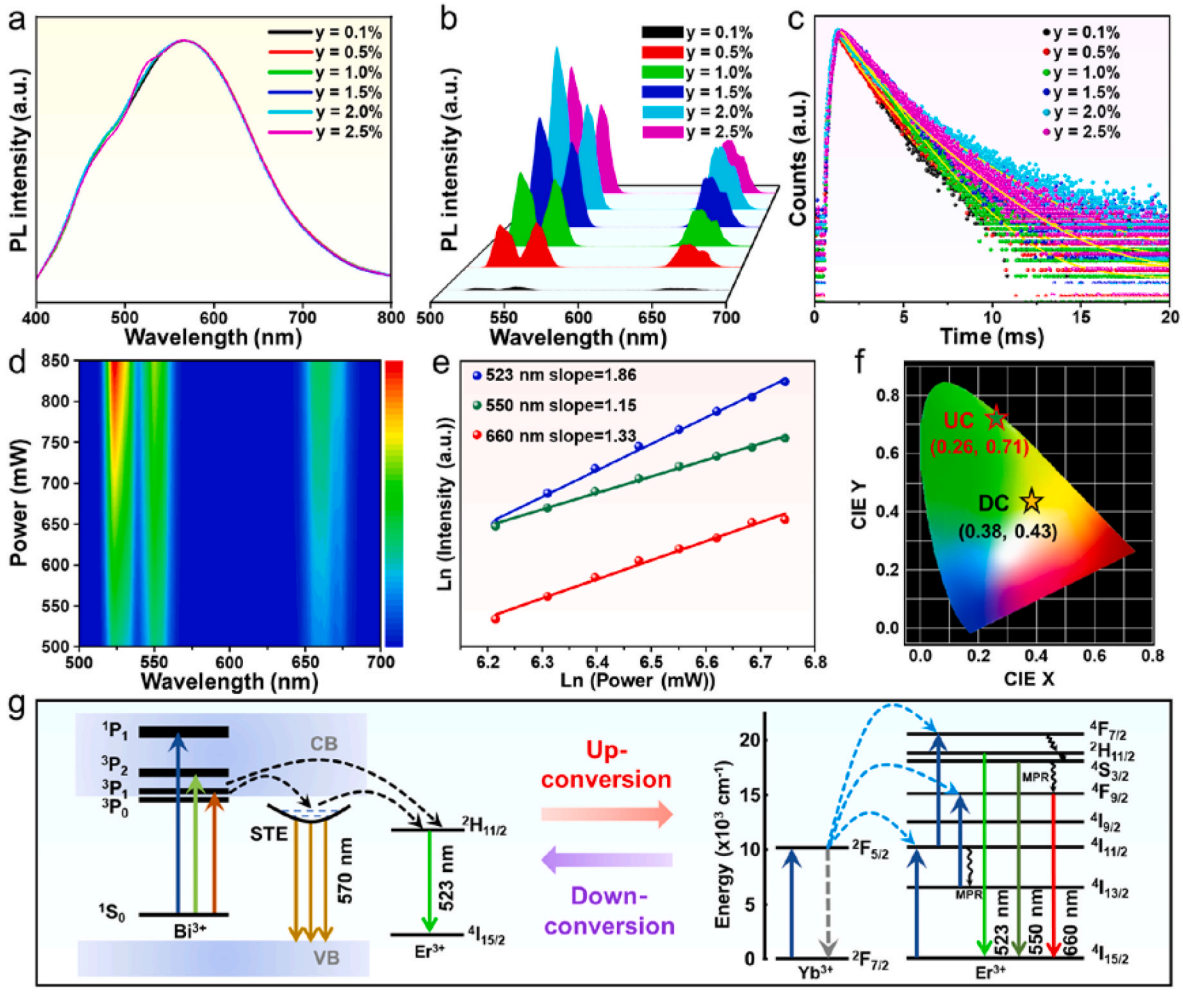

Fig. 6. (a) DC (365 nm excitation) and (b) UC (980 nm excitation) PL spectra of CAIBC:(10%-y)Yb,yEr/PVDF CFs as the Er^{3+} content increased. (c) Time-resolved PL spectra and fitted curves for CFs with different Er^{3+} content. (d) UC PL spectra of CAIBC:8%Yb,2%Er/PVDF CFs under 980 nm pumping with different laser powers. (e) Double logarithmic curves of green and red UC PL intensity. (f) The CIE color coordinates corresponding to the DC and UC PL of CAIBC:8%Yb,2%Er/PVDF CFs respectively. (g) Energy-level diagram of CAIBC:8%Yb,2%Er/PVDF CFs and the DC and UC PL mechanism.

of the green radiation improved significantly from 1.33 ms to 2.15 ms as the Er^{3+} content increased (Table S2). This mainly stemmed from the fact that different doping ratios of rare-earth ions would directly determine the construction of the internal energy levels of CAIBC:(10%-y)Yb,yEr, allowing more electrons to complete the transfer between the rare-earth energy levels, thereby emitting photons of different wavelength, which has also been reported in the UC PL properties of $Cs_2NaInCl_6$:Yb^{3+},x%Er^{3+} crystals [43–45]. Similarly, the PL decay lifetime of CAIBC:7.5%Yb,2.5%Er/PVDF CFs was shortened when the Er^{3+} content further increased owing to the concentration quenching effect, which coincided with the change in UC PL intensity. After that, a comprehensive analysis of the luminescence process and mechanism for CAIBC:8%Yb,2%Er/PVDF CFs with optimal UC PL performance was conducted. Insight into the multi-photon process of CAIBC:8%Yb,2%Er/PVDF CFs by plotting its UC PL spectrum under 980 nm pumping with different laser power (Fig. 6d). In general, the UC PL intensity (I) was proportional to the excitation power (P) [50,51], which was expressed in function as.

$$I \propto P^n$$

where n was the number of photons to be absorbed for each UC emission. The results revealed that the slopes of the linear fitting of the three emission peaks were 1.86, 1.15 and 1.33, respectively (Fig. 6e), indicating the existence of two photon absorption processes during the UC PL. It was well known that the UC process of rare-earth ions are relatively complex, and the energy transfer between multiple energy levels was described in order to get a clear view on the UC PL mechanism of CAIBC:8%Yb,2%Er/PVDF CFs (Fig. 6g). Firstly, benefiting from the large absorption cross section of the Yb^{3+} ions at the 980 nm band, the Yb^{3+} ions was excited from the ground state $^2F_{7/2}$ to $^2F_{5/2}$ after absorbing one 980 nm infrared photon, which then transferred energy to the ground state Er^{3+} ions, and excited it to $^4I_{11/2}$ state. The process as shown below

$$^2F_{5/2}\,(Yb^{3+}) + {}^4I_{15/2}\,(Er^{3+}) \rightarrow {}^2F_{7/2}\,(Yb^{3+}) + {}^4I_{11/2}\,(Er^{3+})$$

Subsequently, most of the Er^{3+} ions in the $^4I_{11/2}$ state will again absorb the energy of the Yb^{3+} ions and transition to the $^4F_{7/2}$ state of Er^{3+} ions. The process as shown below

$$^2F_{5/2}\,(Yb^{3+}) + {}^4I_{11/2}\,(Er^{3+}) \rightarrow {}^2F_{7/2}\,(Yb^{3+}) + {}^4F_{7/2}\,(Er^{3+})$$

Moreover, a non-radiative multiphoton relaxation (MPR) process took place between the $^4F_{7/2}$ state and the $^2H_{11/2}$/$^4S_{3/2}$ state of the Er^{3+} ion. Ultimately, the distinct green fluorescence at 523 nm and 550 nm can be observed with the naked eye through the $^2H_{11/2}$ state and $^4S_{3/2}$ state transition to the ground state ($^4I_{15/2}$), respectively. However, the part of the Er^{3+} ions in the $^4I_{11/2}$ state non-radiative MPR to the $^4I_{13/2}$ state, which was further excited to the $^4F_{9/2}$ state by Yb^{3+}→Er^{3+}. Additionally, some of the Er^{3+} ions at the $^2H_{11/2}$/$^4S_{3/2}$ state can also reached $^4F_{9/2}$ state by MPR. Eventually, the transition from the $^4F_{9/2}$

state to the ground state ($^4I_{15/2}$) allowed the detection of the red-light emission at 660 nm, but its intensity was so poor that the emission could not be observed by the naked eye. In summary, CAIBC:8%Yb,2% Er/PVDF CFs exhibited orange light under 365 nm UV excitation and green light under 980 nm IR excitation, respectively. The two different fluorescence identifications allowed the security level of anti-counterfeiting to be increased, greatly promoting the application of lead-free DPs in the field of multimodal fluorescent anti-counterfeiting.

Subsequently, the optical properties of CAIBC:8%Yb,2%Er/PVDF CFs were recorded under various extreme environments, so that its long-term stability could be assessed for application in the field of anti-counterfeit printing. It is well known that the luminous intensity of fluorescent materials is most obviously influenced by the environmental temperature, so the temperature-dependent fluorescence variation is of great significance for the anti-counterfeiting security of luminescent materials. Here, the changes in DC and UC PL spectra of CAIBC:8% Yb,2%Er/PVDF CFs were recorded at different temperatures. It can be seen that the DC PL intensity of CAIBC:8%Yb,2%Er/PVDF CFs weakened with the temperature increasing (Fig. 7a), which was consistent with the thermal quenching behavior of most fluorescent materials [52,53]. However, an obvious green emission peak was displayed at 523 nm with the temperature continuously elevated, which was derived from the $^2H_{11/2} \rightarrow {}^4I_{15/2}$ transition of Er^{3+}. The phenomenon was attributed to the difference in thermal quenching behaviors between the self-trapped excitons emission of the host and the sharp line emission of the rare earth ions, a similar phenomenon was also reported in previous reports [43]. At the same time, the corresponding color coordinates were transformed from the initial (0.38, 0.43) to (0.35, 0.47) (Fig. 7c). In contrast, the UC PL spectra of CAIBC:8%Yb,2%Er/PVDF CFs under 980 nm excitation showed fluorescence emission from the $^2H_{11/2} \rightarrow {}^4I_{15/2}$ (523 nm), $^4S_{3/2} \rightarrow {}^4I_{15/2}$ (550 nm), and $^4F_{9/2} \rightarrow {}^4I_{15/2}$ (660 nm) transitions were very sensitive to temperature (Fig. 7b). Among them, the emission intensity of the $^2H_{11/2} \rightarrow {}^4I_{15/2}$ (523 nm) transition gradually enhanced, while the emission intensity of the $^4S_{3/2} \rightarrow {}^4I_{15/2}$ (550 nm) and $^4F_{9/2} \rightarrow {}^4I_{15/2}$ (660 nm) transitions was reduced, which resulted from the thermal repopulation of the electrons in the thermally coupled $^2H_{11/2}$ and $^4S_{3/2}$ states [54]. Correspondingly, its color coordinates were transformed from (026, 0.71) to (0.17, 0.78) (Fig. 7d). In summary, the dynamic variation in fluorescence intensity of CAIBC:8%Yb,2%Er/PVDF CFs under different temperatures can also be utilized to achieve cryptographic processing of information, thereby more effectively supporting the development of multimodal fluorescence anti-counterfeiting printing technology. In addition, the optical stability of CAIBC:8%Yb,2% Er/PVDF CFs and the durability of the optical anti-counterfeiting mark were tested under extreme high humidity conditions and atmospheric environment, respectively. The results showed that the fluorescence intensity of DC and UC PL intensities of CAIBC:8%Yb,2%Er/PVDF CFs was not significantly decayed after being stored in water for more than 60 h (Fig. S7), which was attributed to the effective isolation of external water molecules by the PVDF on the surface. At the same time, the printed anti-counterfeiting mark was exposed under atmospheric conditions, and its optical properties did not show any noticeable change

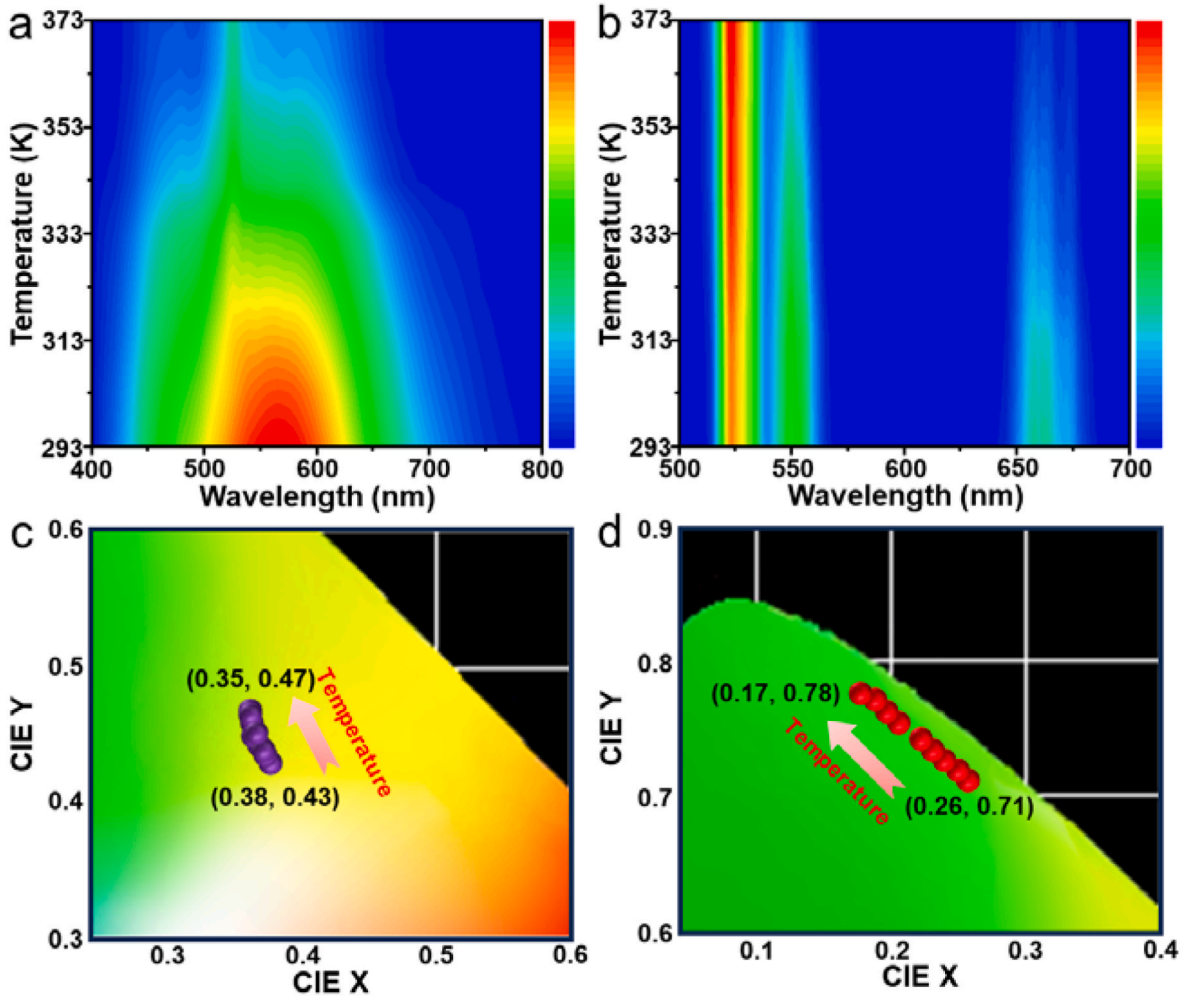

Fig. 7. (a, b) Temperature-dependent DC and UC spectra of CAIBC:8%Yb,2%Er/PVDF CFs under 365 nm and 980 nm excitations, respectively. (c, d) Corresponding CIE color coordinate changes of CAIBC:8%Yb,2%Er/PVDF CFs.

within 10 days (Fig. S8). Therefore, the stability of CAIBC:8%Yb,2% Er/PVDF CFs can strongly supported its long-term development in the field of anti-counterfeiting printing.

The multimodal fluorescence emission of CAIBC:8%Yb,2%Er/PVDF CFs was well suited to applications in advanced security such as information encryption and anti-counterfeiting technology. In order to meet the requirements of practical applications, the precursor solution of CAIBC:8%Yb,2%Er/PVDF CFs was chosen as the ink, whose high fluidity allowed for processability and suitability for the printing process. Subsequently, the designable fluorescent anti-counterfeiting mark was obtained by a simple, efficient and low-cost screen-printing process and annealing post-treatment (Fig. 8). The QR code mark covering two different types of information was obtained by the above-mentioned anti-counterfeiting printing technology. It can be seen that the QR code displayed a yellow light under 365 nm UV light irradiation, and the QR code scanner allowed the information to be identified as "anti-counterfeiting composite film" under this condition. Afterwards, the QR code was exposed to 980 nm IR light, which indicated the green light, and the QR code scanner obtained the information "lead-free double perovskite material". The QR code displayed completely different fluorescence emission under different excitation sources, which enabled obtaining different encrypted information and ensuring information security. Finally, two anti-counterfeiting techniques have been proposed to enhance the security of fluorescent information. For general anti-counterfeiting techniques, the anti-counterfeiting pattern obtained directly using the precursor solution of CAIBC:8%Yb,2%Er/PVDF CFs showed the same outline (phoenix) under irradiation of UV light and IR light. This technique can only identify information by the difference in fluorescence emission, and its level of security to be lower. Therefore, an encryption anti-counterfeiting technique was proposed, where different patterns in the same message were printed by using precursor solutions of CAIBC/PVDF CFs and CAIBC:8%Yb,2%Er/PVDF CFs respectively. Under 365 nm UV light excitation, the yellow fluorescence of the full logo can be seen, but under 980 nm IR light excitation, the logo can only be partially shown to be green fluorescent, this phenomenon being attributed to the fact that precursor solutions with different fluorescence emissions were adopted. In addition, a distinctive leaf mark was obtained by screen-printing technology, and its instantaneous fluorescence photographs were recorded under different temperature. The results showed that the DC photograph of CAIBC:8%Yb,2%Er/PVDF CFs displayed a gradually decreasing yellow fluorescence emission with the temperature elevated, and the DC fluorescence emission of composite films was already almost unobservable when the temperature was elevated to 373 K. At the same time, the UC photographs of CAIBC:8% Yb,2%Er/PVDF CFs showed that its green fluorescence emission remained essentially unchanged, and the UC fluorescence emission of composite films was continuously displayed green when the temperature was raised to 373 K. The above tests demonstrated that utilizing temperature-dependent changes of fluorescence will enable the security of information to be upgraded again, with multiple encryption methods contributing to the prevention of counterfeit incidents. The above results revealed that CAIBC:8%Yb,2%Er/PVDF CFs had excellent performance in the field of anti-counterfeiting, and it was suitable for current multimodal anti-counterfeiting applications, which will provide new ways and important insights for the safeguarding of confidential information.

3. Conclusions

In summary, a convenient and low-cost in-situ growth strategy has been proposed to obtain lead-free DP/PVDF CFs with high quality on a large scale by annealing at 180 °C for 1 h. Subsequently, $Cs_2AgIn_{0.9}Bi_{0.1}Cl_6$/PVDF CFs with excellent down-conversion optical properties was achieved by in situ doping of In^{3+}, which emitted a bright orange under UV light radiation. Afterwards, the expansion of the UC optical properties of $Cs_2AgIn_{0.9}Bi_{0.1}Cl_6$/PVDF CFs was accomplished by hybrid in situ doping with Yb^{3+} and Er^{3+}. $Cs_2AgIn_{0.9}Bi_{0.1}Cl_6$:8%Yb,2% Er/PVDF CFs was able to displayed a green visible to the naked eye under IR light radiation, and its DC fluorescence emission was unaffected. Moreover, the change of DC and UC PL spectra of

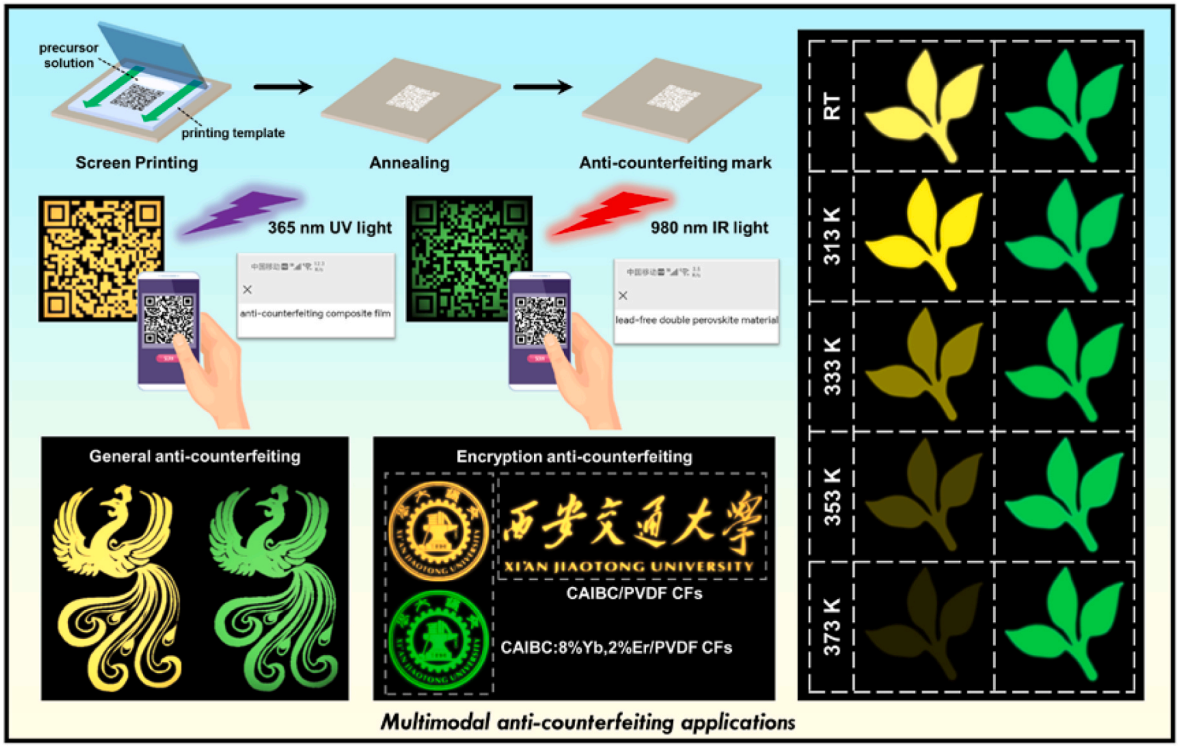

Fig. 8. Schematic diagram of a screen-printing procedure employing a precursor solution of CAIBC:8%Yb,2%Er/PVDF CFs as the pigment and a demonstration of multimodal anti-counterfeiting applications.

$Cs_2AgIn_{0.9}Bi_{0.1}Cl_6$:8%Yb,2%Er/PVDF CFs under different temperatures was recorded, and the DC fluorescence intensity was very sensitive to the temperature, while UC maintained green fluorescence emission all the time, so that the re-encryption of anti-counterfeit mark can be achieved through the identification of fluorescence component under different temperatures. This fluorescence emission relying on the excitation light source as well as the environmental temperature change allowed $Cs_2AgIn_{0.9}Bi_{0.1}Cl_6$:8%Yb,2%Er/PVDF CFs to take their place in the field of multimodal fluorescence anti-counterfeiting, followed by screen printing technology to get a variety of different encrypted anti-counterfeiting patterns, whose excellent performance again guaranteed the security of the information, while also expanding the application prospects of lead-free DP materials in subsequent commercial development.

CRediT authorship contribution statement

Jindou Shi: Conceptualization, Data curation, Formal analysis, Investigation, Methodology, Project administration, Resources, Writing - original draft. **Zeyu Wang:** Conceptualization, Writing - review & editing. **Nikolai V. Gaponenko:** Supervision. **Zheyuan Da:** Supervision. **Chen Zhang:** Supervision. **Junnan Wang:** Supervision. **Yongqiang Ji:** Supervision. **Qing Yao:** Supervision. **Yusong Ding:** Supervision. **Minqiang Wang:** Supervision. **Youlong Xu:** Supervision.

Declaration of competing interest

The authors declare that they have no known competing financial interests or personal relationships that could have appeared to influence the work reported in this paper.

Data availability

No data was used for the research described in the article.

Acknowledgements

This work was supported by the National Key R&D Program of China (2022YFE0122500 and 2019YFB1503200), National Natural Science Foundation of China (NSFC, 52161145103 and 61774124), and 111 Program (No. B14040), and Shaanxi Provincial Key Research and Development Program (No.2021GXLH-Z-084). The authors thank Ms. Chenyu Liang at Instrument Anaysis Center of Xi'an Jiaotong University for her the help with the XPS analysis.

Appendix A. Supplementary data

Supplementary data to this article can be found online at https://doi.org/10.1016/j.mtchem.2023.101874.

References

[1] a Y. Sun, X.X. Le, S.Y. Zhou, T. Chen, Recent progress in smart polymeric gel-based information storage for anti-counterfeiting, Adv. Mater. 34 (41) (2022); b Y. Sun, X.X. Le, S.Y. Zhou, T. Chen, Recent progress in smart polymeric gel-based information storage for anti-counterfeiting, Adv. Mater. 34 (2022), 2201262, https://doi.org/10.1002/Adma.202201262.

[2] K. Ludasi, O. Jojart-Laczkovich, T. Sovany, B. Hopp, T. Smausz, A. Andrasik, T. Gera, Z. Kovacs, G. Regdon, Anti-counterfeiting protection, personalized medicines-Development of 2D identification methods using laser technology, Int. J. Pharm. (Amst.) 605 (2021), 120793, https://doi.org/10.1016/j.ijpharm.2021.120793.

[3] D.F. Hu, W.J. Xu, G. Wang, K. Liu, Z.L. Wang, Q.Y. Shi, S.M. Lin, Z.S. Liu, Y. Fang, A mild-stimuli-responsive fluorescent molecular system enables multilevel anti-counterfeiting and highly adaptable temperature monitoring, Adv. Funct. Mater. 32 (2022), 2207895, https://doi.org/10.1002/Adfm.202207895.

[4] Z.M. Deng, L.L. Li, P.P. Tang, C.Y. Jiao, Z.Z. Yu, C.M. Koo, H.B. Zhang, Controllable surface-grafted MXene inks for electromagnetic wave modulation and infrared anti-counterfeiting applications, ACS Nano 16 (2022) 16976–16986, https://doi.org/10.1021/acsnano.2c07084.

[5] H. Zhou, J.J. Han, J. Cuan, Y. Zhou, Responsive luminescent MOF materials for advanced anticounterfeiting, Chem. Eng. J. 431 (2022), 134170, https://doi.org/10.1016/J.Cej.2021.134170.

[6] H. Wang, Z. Qin, L.L. Huang, Y.F. Li, R.Z. Zhao, H.Q. Zhou, H.Y. He, J.Q. Zhang, S. B. Qu, Metasurface with dynamic chiral meta-atoms for spin multiplexing hologram and low observable reflection, Photonix 3 (2022) 10, https://doi.org/10.1186/S43074-022-00057-1.

[7] Y.H. Lin, H.K. Zhang, J.Y. Feng, B.R. Shi, M.Y. Zhang, Y.X. Han, W.J. Wen, T. Y. Zhang, Y.B. Qi, J.B. Wu, Unclonable micro-texture with clonable micro-shape towards rapid, convenient, and low-cost fluorescent anti-counterfeiting labels, Small 17 (2021), 2100244, https://doi.org/10.1002/Smll.202100244.

[8] C. Li, X.S. Liu, Y.L. Han, Q. Guo, W.B. Yang, Q. Liu, B. Song, X.L. Zheng, S.Y. Tao, Ultra-stable anti-counterfeiting materials inspired by water stains, Cell Reports Physical Science 2 (2021), 100571, https://doi.org/10.1016/J.Xcrp.2021.100571.

[9] R. An, J.Y. Hao, S.Y. Song, H.J. Zhang, J. Feng, X.Y. Wang, H.Z. Sun, Multi-responsive 0D organic-inorganic hybrid cuprous bromides constructed via ultra-facile approaches for multimodal luminescent anti-counterfeiting, Adv. Opt. Mater. (2023), 2202596, https://doi.org/10.1002/adom.202202596.

[10] S.Y. Tian, H. Zhang, X.X. Yang, L.L. Yang, Q.H. Min, H.Q. Ma, X. Yu, J.B. Qiu, X. H. Xu, A dynamic three-path authenticating model for anti-counterfeiting in a single host of $CaAl_2Si_2O_8$, Chem. Eng. J. 412 (2021), 128695, https://doi.org/10.1016/J.Cej.2021.128695.

[11] F.S. Zhang, Q.Y. Li, C.L. Wang, D.D. Wang, M.Y. Song, Z. Li, X.Y. Xue, G. Zhang, G. Y. Qing, Multimodal, Convertible, and chiral optical films for anti-counterfeiting labels, Adv. Funct. Mater. 32 (2022), 2204487, https://doi.org/10.1002/Adfm.202204487.

[12] C.C. Wang, Y.Q. Huang, E. Heydari, X.L. Yang, S.Q. Xu, G.X. Bai, Dual-mode optical ratiometric thermometer based on rare earth ions doped perovskite oxides with tunable luminescence, Ceram. Int. 48 (2022) 12578–12584, https://doi.org/10.1016/j.ceramint.2022.01.125.

[13] D.D. Yang, Z.X. Peng, X. Guo, S.Q. Qiao, P. Zhao, Q.Q. Zhan, J.R. Qiu, Z.M. Yang, G.P. Dong, Tunable light polarization information from single upconverting fluoride microcrystal, Adv. Opt. Mater. 9 (2021), 2100044, https://doi.org/10.1002/Adom.202100044.

[14] A.O. Larin, L.N. Dvoretckaia, A.M. Mozharov, I.S. Mukhin, A.B. Cherepakhin, I. I. Shishkin, E.I. Ageev, D.A. Zuev, Luminescent erbium-doped silicon thin films for advanced anti-counterfeit labels, Adv. Mater. 33 (2021), 2005886, https://doi.org/10.1002/Adma.202005886.

[15] D.W. Zhang, W. Zhou, Q.L. Liu, Z.G. Xia, $CH_3NH_3PbBr_3$ perovskite nanocrystals encapsulated in lanthanide metal-organic frameworks as a photoluminescence converter for anti-counterfeiting, ACS Appl. Mater. Interfaces 10 (2018) 27875–27884, https://doi.org/10.1021/acsami.8b10517.

[16] X.W. Yu, K.K. Liu, H.Y. Zhang, B.L. Wang, W.Y. Ma, J.Y. Li, J.H. Yu, Carbon dots-in-EuAPO-5 zeolite: triple-emission for multilevel luminescence anti-counterfeiting, Small 17 (2021), 2103374, https://doi.org/10.1002/Smll.202103374.

[17] W.T. Hong, H.K. Yang, Anti-counterfeiting application of fluorescent carbon dots derived from wasted coffee grounds, Optik 241 (2021), 166449, https://doi.org/10.1016/J.Ijleo.2021.166449.

[18] S.K. Gupta, K. Sudarshan, R.M. Kadam, Optical nanomaterials with focus on rare earth doped oxide: a Review, Mater. Today Commun. 27 (2021), 102277, https://doi.org/10.1016/J.Mtcomm.2021.102277.

[19] R. Shi, C.D.S. Brites, L.D. Carlos, Hexagonal-phase $NaREF_4$ upconversion nanocrystals: the matter of crystal structure, Nanoscale 13 (2021) 19771–19782, https://doi.org/10.1039/d1nr04209b.

[20] S.S. Yuan, J. Wang, Y. Xiang, S.S. Zheng, Y.H. Wu, J.L. Liu, X.H. Zhu, Y. Zhang, Shedding light on luminescent janus nanoparticles: from synthesis to photoluminescence and applications, Small 18 (2022), 2200020, https://doi.org/10.1002/Smll.202200020.

[21] F. Khan, T. Alshahrani, I. Fareed, M. Al-Rasheidi, N. Ahmad, A. Al-Ahmed, M. H. Zahir, J.H. Kim, Impact of solvent on the downconversion efficiency of the N-GQDs/PMMA layer: application in CIGS solar cells, Optik 253 (2022), 168569, https://doi.org/10.1016/J.Ijleo.2022.168569.

[22] T. Kim, D. Shin, M. Kim, H. Kim, E. Cho, M. Choi, J. Kim, E. Jang, S. Jeong, Development of group III-V colloidal quantum dots for optoelectronic applications, ACS Energy Lett. 8 (2022) 447–456, https://doi.org/10.1021/acsenergylett.2c02489.

[23] J.D. Shi, M.Q. Wang, C. Zhang, J.N. Wang, Y. Zhou, Y.L. Xu, N.V. Gaponenko, A. S. Bhatti, In situ fabrication of lead-free double perovskite/polymer composite films for optoelectronic devices and anticounterfeit printing, ACS Appl. Mater. Interfaces 15 (2023) 12383–12392, https://doi.org/10.1021/acsami.2c22752.

[24] X. Li, D.D. Wang, Y. Zhong, F. Jiang, D.Q. Zhao, S.Q. Sun, P. Lu, M. Lu, Z.Y. Wang, Z.N. Wu, Y.B. Gao, Y. Zhang, W.W. Yu, X. Bai, Halide double perovskite nanocrystals doped with rare-earth ions for multifunctional applications, Adv. Sci. (2023), 2207571, https://doi.org/10.1002/advs.202207571.

[25] J. Shi, M. Wang, C. Zhang, J. Wang, Y. Zhou, Y. Xu, N.V. Gaponenko, Enhanced stability of lead-free double perovskite $Cs_2Na_{1-x}Bi_{1-x}Mn_{2x}Cl_6$ microcrystals and their optoelectronic devices under high humidity environment by SiO_2 encapsulation, Mater. Today Chem. 29 (2023), 101480, https://doi.org/10.1016/j.mtchem.2023.101480.

[26] R.X. Wu, P.G. Han, D.Y. Zheng, J.F. Zhang, S.Q. Yang, Y. Zhao, X.Y. Miao, K.L. Han, All-inorganic rare-earth-based double perovskite nanocrystals with near-infrared emission, Laser Photon. Rev. 15 (2021), 2100218, https://doi.org/10.1002/Lpor.202100218.

[27] Z.C. Zeng, B.L. Huang, X. Wang, L. Lu, Q.Y. Lu, M.Z. Sun, T. Wu, T.F. Ma, J. Xu, Y. S. Xu, S. Wang, Y.P. Du, C.H. Yan, Multimodal luminescent $Yb^{3+}/Er^{3+}/Bi^{3+}$-doped

perovskite single crystals for X-ray detection and anti-counterfeiting, Adv. Mater. 32 (2020), 2004506, https://doi.org/10.1002/Adma.202004506.
[28] W.S. Jiang, R.J. Sun, S. Wang, Y. Yu, L.H. Qi, K. Pan, Improved optical properties of lead-free double perovskite $Cs_2NaBiCl_6$ nanocrystal via K ions doping, J. Alloys Compd. 960 (2023), 170871, https://doi.org/10.1016/j.jallcom.2023.170871.
[29] R.J. Sun, W.S. Jiang, S. Wang, W.J. Cui, L.H. Qi, K. Pan, K-alloyed lead-free double-Perovskite $Cs_2AgBiBr_6$ nanocrystals for use in light-emitting diodes, ACS Appl. Nano Mater. 6 (2023), https://doi.org/10.1021/acsanm.3c03020, 15247−15254.
[30] S. Wang, Y. Xie, W. Jiang, B. Liu, K. Shi, K. Pan, Incorporation sodium ions into monodisperse lead-free double perovskite $Cs_2AgBiCl_6$ nanocrystals to improve optical properties, Chin. Chem. Lett. (2023), 108521, https://doi.org/10.1016/j.cclet.2023.108521.
[31] J.D. Shi, M.Q. Wang, C. Zhang, J.N. Wang, Y. Zhou, Y.L. Xu, N.V. Gaponenko, Enhanced stability of lead-free double perovskite $Cs_2AgIn_xBi_{1-x}Cl_6$ crystals under a high humidity environment by surface capping treatment, J. Mater. Chem. C 11 (2023) 4742–4752, https://doi.org/10.1039/d2tc05420e.
[32] Y. Bekenstein, J.C. Dahl, J.M. Huang, W.T. Osowiecki, J.K. Swabeck, E.M. Chan, P. D. Yang, A.P. Alivisatos, The making and breaking of lead-free double perovskite nanocrystals of cesium silver-bismuth halide compositions, Nano Lett. 18 (2018) 3502–3508, https://doi.org/10.1021/acs.nanolett.8b00560.
[33] B. Yang, J.S. Chen, F. Hong, X. Mao, K.B. Zheng, S.Q. Yang, Y.J. Li, T. Pullerits, W. Q. Deng, K.L. Han, Lead-free, air-stable all-inorganic cesium bismuth halide perovskite Nanocrystals, Angew. Chem., Int. Ed. 56 (41) (2017) 12471–12475, https://doi.org/10.1002/anie.201704739.
[34] B. Yang, J.S. Chen, S.Q. Yang, F. Hong, L. Sun, P.G. Han, T. Pullerits, W.Q. Deng, K. L. Han, Lead-free silver-bismuth halide double perovskite nanocrystals, Angew. Chem., Int. Ed. 57 (2018) 5359–5363, https://doi.org/10.1002/anie.201800660.
[35] B. Yang, X. Mao, F. Hong, W.W. Meng, Y.X. Tang, X.S. Xia, S.Q. Yang, W.Q. Deng, K.L. Han, Lead-free direct band gap double-perovskite nanocrystals with bright dual-color emission, J. Am. Chem. Soc. 140 (2018) 17001–17006, https://doi.org/10.1021/jacs.8b07424.
[36] W.W. Meng, X.M. Wang, Z.W. Xiao, J.B. Wang, D.B. Mitzi, Y.F. Yan, Parity-forbidden transitions and their impact on the optical absorption properties of lead-free metal halide perovskites and double perovskites, J. Phys. Chem. Lett. 8 (2017) 2999–3007, https://doi.org/10.1021/acs.jpclett.7b01042.
[37] M.M. Yao, L. Wang, J.S. Yao, K.H. Wang, C. Chen, B.S. Zhu, J.N. Yang, J.J. Wang, W.P. Xu, Q. Zhang, H.B. Yao, Improving lead-free double perovskite $Cs_2NaBiCl_6$ nanocrystal optical properties via ion doping, Adv. Opt. Mater. 8 (2020), 1901919, https://doi.org/10.1002/Adom.201901919.
[38] J.D. Majher, M.B. Gray, T.A. Strom, P.M. Woodward, $CsNaBiCl_6:Mn^{2+}$ - a new orange-red halide double perovskite phosphor, Chem. Mater. 31 (5) (2019) 1738–1744, https://doi.org/10.1021/acs.chemmater.8b05280.
[39] G.Y. Zhang, D.Y. Wang, B.B. Lou, C.G. Ma, A. Meijerink, Y.H. Wang, Efficient broadband near-infrared emission from lead-free halide double perovskite single crystal, Angew. Chem., Int. Ed. 61 (33) (2022), https://doi.org/10.1002/anie.202207454.
[40] G. Volonakis, A.A. Haghighirad, R.L. Milot, W.H. Sio, M.R. Filip, B. Wenger, M. B. Johnston, L.M. Herz, H.J. Snaith, F. Giustino, $Cs_2InAgCl_6$: a new lead-free halide double perovskite with direct band gap, J. Phys. Chem. Lett. 8 (4) (2017) 772–778, https://doi.org/10.1021/acs.jpclett.6b02682.
[41] J.J. Luo, S.R. Li, H.D. Wu, Y. Zhou, Y. Li, J. Liu, J.H. Li, K.H. Li, F. Yi, G.D. Niu, J. Tang, $Cs_2AgInCl_6$ double perovskite single crystals: parity forbidden transitions and their application for sensitive and fast UV photodetectors, ACS Photonics 5 (2) (2018) 398–405, https://doi.org/10.1021/acsphotonics.7b00837.
[42] B.A. Connor, L. Leppert, M.D. Smith, J.B. Neaton, H.I. Karunadasa, Layered halide double perovskites: dimensional reduction of $Cs_2AgBiBr_6$, J. Am. Chem. Soc. 140 (15) (2018) 5235–5240, https://doi.org/10.1021/jacs.8b01543.
[43] Y. Li, C. Chen, M. Jin, J. Xiang, J. Tang, Z. Li, W. Chen, J. Zheng, C. Guo, External-field-dependent tunable emissions of Er^{3+}-In^{3+} Co-doped $Cs_2AgBiCl_6$ for applications in anti-counterfeiting, Mater Today Phys 27 (2022), 100830, https://doi.org/10.1016/J.Mtphys.2022.100830.
[44] Y.H. Shi, X.Z. Zhang, X.J. Wang, Y.H. Zhang, Pure green upconversion from a multicolor downshifting perovskite crystal, Adv. Opt. Mater. 11 (10) (2023), 2202704, https://doi.org/10.1002/adom.202202704.
[45] W.Y. Ge, J.D. Shi, M.M. Xu, X.L. Chen, J.F. Zhu, Red upconversion luminescence (UCL) properties in one-dimensional $Yb_2Ti_2O_7$: Er nanofibers via an electrospinning route, J. Alloys Compd. 788 (2019) 993–999, https://doi.org/10.1016/j.jallcom.2019.02.319.
[46] P. Ramasamy, P. Chandra, S.W. Rhee, J. Kim, Enhanced upconversion luminescence in NaGdF:Yb,Er nanocrystals by Fe^{3+} doping and their application in bioimaging, Nanoscale 5 (18) (2013) 8711–8717, https://doi.org/10.1039/c3nr01608k.
[47] S. Namagal, N.V. Jaya, N. Nithyaa, M. Muralidharan, S. Venkatesh, Upconversion of NaYF: Yb, Er nanoparticles co-doped with Zr^{4+} for magnetic phase transition and biomedical imaging applications, J. Inorg. Organomet. Polym. 32 (8) (2022) 3128–3140, https://doi.org/10.1007/s10904-022-02342-9.
[48] J.D. Shi, W.Y. Ge, M.M. Xu, J.F. Zhu, $Bi_2Ti_2O_7$ nanoparticles: an oxide based upconversion luminescence host by a simple sol-gel route, J. Lumin. 213 (2019) 15–18, https://doi.org/10.1016/j.jlumin.2019.05.005.
[49] B. Chen, F. Wang, Combating concentration quenching in upconversion nanoparticles, Accounts Chem. Res. 53 (2020) 358–367, https://doi.org/10.1021/acs.accounts.9b00453.
[50] C. Li, X. Zhang, Y.Q. Yang, V.C. Onah, W.L. Yang, Z. Leng, X.L. Jiang, G.Y. Xu, H. Lin, C. Li, D.F. Zhou, F.M. Zeng, Effect of Yb/Er/Li on structure and up-conversion luminescence properties of $NaSc(WO_4)_2$, J. Mater. Sci. Mater. Electron. 33 (2022) 12259–12270, https://doi.org/10.1007/s10854-022-08185-x.
[51] W.Y. Ge, M.M. Xu, J.D. Shi, J.F. Zhu, Y.X. Li, Highly temperature-sensitive and blue upconversion luminescence properties of $Bi_2Ti_2O_7:Tm^{3+}/Yb^{3+}$ nanofibers by electrospinning, Chem. Eng. J. 391 (2020), 123546, https://doi.org/10.1016/J.Cej.2019.123546.
[52] J.D. Shi, W.Y. Ge, W.X. Gao, M.M. Xu, J.F. Zhu, Y.X. Li, Enhanced thermal stability of halide perovskite $CsPbX_3$ nanocrystals by a facile TPU encapsulation, Adv. Opt. Mater. 8 (4) (2020), 1901516, https://doi.org/10.1002/Adom.201901516.
[53] J.D. Shi, W.Y. Ge, Y. Tian, M.M. Xu, W.X. Gao, Y.T. Wu, Enhanced stability of all-inorganic perovskite light-emitting diodes by a facile liquid annealing strategy, Small 17 (14) (2021), 2006568, https://doi.org/10.1002/Smll.202006568.
[54] J.S. Sun, Z.Y. Zhang, H. Suo, Y.H. Chen, J.M. Xiang, C.F. Guo, Temperature self-monitoring photothermal nano-particles of Er/Yb Co-doped zircon-tetragonal $BiVO_4$, Ceram. Int. 47 (1) (2021) 409–415, https://doi.org/10.1016/j.ceramint.2020.08.147.